Tilt scanning interferometry: a numerical simulation benchmark for 3D metrology

Gustavo E. Galizzi,[1,*] Pablo D. Ruiz,[2] and Guillermo H. Kaufmann[1,3]

[1]Instituto de Física Rosario, Blvd. 27 de Febrero 210 bis, S2000EZP, Rosario, Argentina

[2]Wolfson School of Mechanical and Manufacturing Engineering, Loughborough University, LE11 3TU, Loughborough, United Kingdom

[3]Centro Internacional Franco Argentino de Ciencias de la Información y de Sistemas, Blvd. 27 de Febrero 210 bis, S2000EZP, Rosario, Argentina

*Corresponding author: galizzi@ifir-conicet.gov.ar

Received 23 February 2009; accepted 13 April 2009;
posted 14 May 2009 (Doc. ID 107783); published 5 June 2009

Tilt scanning interferometry (TSI) is a novel experimental technique that allows the measurement of multicomponent displacement fields inside the volume of a sample. In this paper, we present a simulation model that allows for the evaluation of the speckle fields recorded in TSI when this technique is applied to the analysis of semitransparent scattering materials. The simulation is based on the convolution of the optical impulsive response of the optical system and the incident field amplitude. Different sections of the simulated imaging system are identified and the corresponding optical impulsive responses are determined. To evaluate the performance of the proposed model, a known internal displacement field as well as the illumination and detection strategies in a real TSI system are numerically simulated. Then, the corresponding depth-resolved out-of-plane and in-plane changes of phase are obtained by means of the data processing algorithm implemented in a TSI system. © 2009 Optical Society of America

OCIS codes: 120.6160, 120.6150, 120.5050, 120.2650, 120.4290, 100.3190.

1. Introduction

There are currently powerful identification approaches to obtain the constitutive parameters of a material from 2D full-field strain measurements. The finite element method can be used to solve the direct problem, starting with initial guesses of the unknown parameters and performing simulations iteratively until the displacements computed at various nodes of the mesh match their experimental counterparts. This is known as finite element model updating (FEMU) [1]. The virtual fields method (VFM) [2–4] is another approach that solves the inverse problem. Given measured strain fields, the stress fields are expressed as a parameterized function of the unknown constitutive parameters. The principle of virtual work is then applied so that the stress fields verify the global equilibrium of the structure. Finally, the use of several virtual fields yields a system of equations that involves the unknown parameters and which leads to the solution.

Traditionally, digital speckle pattern interferometry (DSPI) [5,6] has been a standard technique for obtaining accurate and fast measurements of shape [7] and displacement fields over the surface of optically rough objects [8]. Deflectometry was used to measure 2D displacements to find the damping material properties of isotropic vibrating plates [9]. The grid method was also used to measure 2D displacements to find stiffness parameters of glass epoxy beams [10] and 2D digital image correlation and FEMU were used to measure elasto-visco-plastic parameters on steel at high strain rates [11]. All these cases relied on surface measurements to characterize material constitutive parameters under the assumption that they do not vary from point to point within the material.

0003-6935/09/173184-08$15.00/0

To map the volumetric distributions of those parameters, however, full-field 3D measurements are required. This is relevant when heterogeneous materials are studied at a scale in which different constituents are resolved, e.g., the fibers and the matrix in a composite material, different structural biological tissues, or multimaterial structures. Techniques that allow us to measure multicomponent displacement fields inside the volume of the material will enable us to determine nonuniform distributions of constitutive parameters, which is essential to accurately predict mechanical behavior.

A broad range of methods to measure internal structure and displacement fields have been developed in the last few decades such as neutron and x-ray diffraction, photoelastic tomography (PT) [12,13], phase contrast magnetic resonance imaging (PCMRI) [14,15], and 3D digital image correlation (DIC) using data acquired with x-ray computed tomography (XCT) [16] and optical coherence tomography (OCT) [17–20]. These are all complementary techniques that are appropriate to study different materials: PT, for example, is suitable only for materials that exhibit photoelasticity; PCMRI requires significant water or fat content in the sample, and neutron diffraction relies on the crystalline structure of the material.

Recently, Ruiz *et al.* [21] introduced a different approach to measure depth-resolved displacements within semitransparent scattering materials. The technique, known as tilt scanning interferometry (TSI), is a form of optical diffraction tomography [22] and is based on tilting the illuminating beam during the acquisition of sequences of speckle interferograms. This provides the necessary phase shifts that encode depth within the material, thus enabling the reconstruction of the object structure and the evaluation of internal displacements through optical phase measurements. 3D displacement fields have been measured with out-of-plane and one in-plane sensitivities, but all three components of the displacement vector can be achieved.

These features of TSI make it particularly attractive for providing the necessary 3D data for the identification of constitutive parameters within semitransparent scattering materials. Changes in the optical phase, however, not only arise as a result of displacement of the scattering centers within the material. There are other factors that introduce phase changes: (a) photoelastic coupling, i.e., stress induced changes of the refractive index; (b) changes in the curvature of the object surface in response to the applied loads, which leads to changes in the shape of the illumination wavefront travelling within the material; (c) refractive index gradients, which will have a similar effect and are usually unknown; (d) and finally, multiple scattering and light absorption, which will affect the phase noise and therefore the uncertainties in the measured displacement and strain fields.

If strain distributions are to be estimated from TSI phase measurements, then the relative importance of these other factors in the measured phase need to be assessed. This could be done experimentally with a well-controlled, well-known test object (phantom) and using validation techniques to support the measurements. This is certainly not an easy task, and results on one material would not be valid for different materials. Another approach consists in developing a numerical model in which the object and the interferometer are simulated. While the object deformation can be readily modeled using finite element analysis by using any available commercial package, a numerical model of the interferometer needs to be developed.

The purpose of this paper is, therefore, to present a numerical model of the TSI technique when it is applied to the analysis of semitransparent scattering materials. We start by simulating an incident optical field scattered within the object and imaged onto a 2D detector array. This is the core contribution of the paper and is fully described in Section 2. In Section 3 the TSI system is modeled, including image acquisition and the data processing that leads to the evaluation of phase changes. In Section 4, we test the models using a simple object geometry and known internal displacement fields with in-plane and out-of-plane components. Finally, a discussion of the advantages and limitations is presented in Section 5, including comments on further developments.

2. Numerical Simulation of Subjective Speckle Fields from a Semi-Transparent Scattering Volume

Considering an optical system under the paraxial approximation, the field amplitude u_o detected at its output plane can be evaluated using the convolution operation as [23,24]

$$u_o = h \otimes u_i, \tag{1}$$

where u_i is the incident optical field amplitude at the input plane and h is the optical impulsive response of the system.

In the spatial frequency domain, Eq. (1) can be rewritten as

$$U_o = HU_i, \tag{2}$$

where U_i, U_o, and H are the Fourier transforms of u_i, u_o, and h, respectively.

Assuming that an arrangement of scattering centers is placed across the input plane and no depolarization effects occur, u_i can be expressed as

$$u_i = \exp[j(\varphi_d + \varphi_s)], \tag{3}$$

where φ_s is a random phase value uniformly distributed in the interval $[-\pi, \pi)$, which represents the random optical path fluctuations introduced by the scattering centers and due to the light propagation through a semitransparent scattering material,

and φ_d is a deterministic phase value that depends on the initial phase of the incident wave and also on the optical path from the light source to the output plane of the system. In the general case, φ_d includes terms introduced by displacement fields produced by the object upon deformation as well as changes in refractive index of the material, e.g., due to stress-optic coupling or temperature. Consequently, the optical field amplitude detected at the output plane of the optical system can be easily computed in the Fourier domain as

$$U_o = \mathrm{FT}(u_o) = H\mathrm{FT}\{\exp[j(\varphi_d + \varphi_s)]\}, \tag{4}$$

where FT stands for the Fourier transform operator and $j = (-1)^{\frac{1}{2}}$ is the imaginary unit.

In a free space propagation configuration, the optical transfer function H_{fs} can be expressed as [23]

$$H_{fs} = \exp(jkd_{fs}) \exp[-j\pi\lambda d_{fs}(f_x^2 + f_y^2)], \tag{5}$$

where d_{fs} is the distance separating the input and output planes, λ is the light wavelength, $k = 2\pi/\lambda$ is the modulus of the wave vector, and (f_x, f_y) are the spatial frequencies in a plane perpendicular to the direction of propagation. In this case, the generated optical field corresponds to an objective speckle pattern.

In a $4f$ system configuration, the optical transfer function H_{4f} is a circular low pass filter defined as

$$H_{4f} = \begin{cases} 1 & \text{if}(f_x^2 + f_y^2)^{\frac{1}{2}} \le \Omega_c \\ 0 & \text{otherwise} \end{cases}, \tag{6}$$

where Ω_c is the cutoff frequency of the filter, which defines the average speckle size [24,25]. As known, Ω_c can be evaluated as [24]

$$\Omega_c = \frac{D_A}{4\lambda f}, \tag{7}$$

where D_A is the diameter of the aperture of the imaging system, f is the focal length of the system, and λ the wavelength of the light. In this case, the generated optical field corresponds to a subjective speckle pattern.

In our simulation, we used a combination of both free space propagation and the $4f$ configuration to model a TSI system. The assumptions of the model are as follows: there is no multiple scattering present, no absorption, and the refractive index variations are only in a scale smaller than the resolution volume of the system given by the lateral and depth resolutions. The latter ensures that scattering is present to give back a signal, but then light propagates as through a medium of uniform refractive index. Additionally, it is supposed that the whole system is immersed in a transparent medium of refractive index $n_0 = 1$.

Figure 1 depicts the simulated imaging system used to numerically generate the speckle distributions. The $4f$ optical configuration is composed by two lenses L_i and L_o, each one with focal length f. Both lenses are separated by a distance $2f$ and the aperture of the imaging system is A. A detector array D is placed at the output plane of the system. The optical transfer function H_{4f} associated with this configuration is defined by Eq. (6). The beam splitter BS is used to combine the scattered light collected from the object with a plane wave, which acts as the reference beam of the interferometer. The sample M is a semitransparent object of uniform refractive index n_M, positioned at a distance d_r behind the input plane of the $4f$ system.

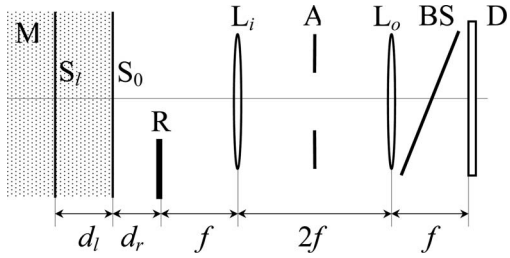

Fig. 1. Imaging system and sample geometry used to simulate the speckle fields used in TSI to measure depth-resolved displacements inside semitransparent scattering materials: L_i and L_o form a $4f$ system; D, detector array; A, aperture of the imaging system; BS, beam splitter; R, reference surface; M, material sample with refractive index n_M.

The free space propagation system is identified by the distance separating the scattering surface and the observation plane. In this case, we can associate one system with the light propagation through the sample from each internal scattering layer S_l to the sample surface S_0, and another from S_0 up to the input plane of the $4f$ optical system.

A rough opaque surface R, called reference surface, is placed at the input plane of the $4f$ system and blocks up a small region of the sample. The reference surface allows for carrier detection and error correction in the TSI system, the latter of which is introduced by nonlinearities of the tilting device or misalignments in the experimental setup.

The optical field amplitude recorded at detector array D, which is generated by the light back-scattered by the sample, can be evaluated by adding the contributions from every scattering layer S_l and the sample surface S_0. Considering that $U_{i_{S_0}}$ and $U_{i_{S_l}}$ are the incident optical field amplitudes in the spatial frequency domain at S_0 and S_l, respectively, the optical field U_{o_M} recorded by the detector array is given by

$$U_{o_M} = H_{4f}H_{fs_0}(U_{i_{S_0}} + \sum_l H_{fs_l}U_{i_{S_l}}), \tag{8}$$

where l identifies each internal scattering layer, H_{4f} is the optical transfer function of the $4f$ system configuration [see Eq. (6)], H_{fs_l} is the transfer function associated to the propagation of the light from S_l through the sample, and H_{fs_0} is the transfer function of the propagation system from the sample surface

up to the input plane of the $4f$ system. These transfer functions can be expressed as [see Eq. (5)]

$$H_{fs_0} = \exp(jkd_r)\exp[-j\pi\lambda d_r(f_x^2+f_y^2)],$$
$$H_{fs_l} = \exp(jkn_M d_l)\exp[-j\pi\lambda n_M d_l(f_x^2+f_y^2)], \quad (9)$$

where d_l is the distance from S_l to S_0.

The optical field amplitude U_{o_R} recorded by detector array D and generated by the light scattered by the reference surface can be evaluated as

$$U_{o_R} = H_{4f}U_{i_R}, \quad (10)$$

where U_{i_R} is the incident optical amplitude over R.

The total optical field U_{o_T} recorded at the detector plane is equal to U_{o_R} where the reference surface blocks up the view of the sample, and to U_{o_M} elsewhere. Finally, a constant term must be added to U_{o_T} to simulate the reference beam of the interferometer.

3. Simulation of the TSI Illumination System and Data Processing

A. TSI Illumination and Acquisition System

Figure 2 shows a schematic diagram that is used in the TSI system to illuminate the sample. The origin of the defined coordinate system (x,y,z) is placed at point O, which lies on reference surface R. R is a rough opaque surface, placed at the region $z=0$ and $y \le 0$. Sample M is a semitransparent object of refractive index n_M located at $z=d_r$ and illuminated by a collimated beam of wavelength λ at an angle θ to the optical axis of the system. In this case, the plane

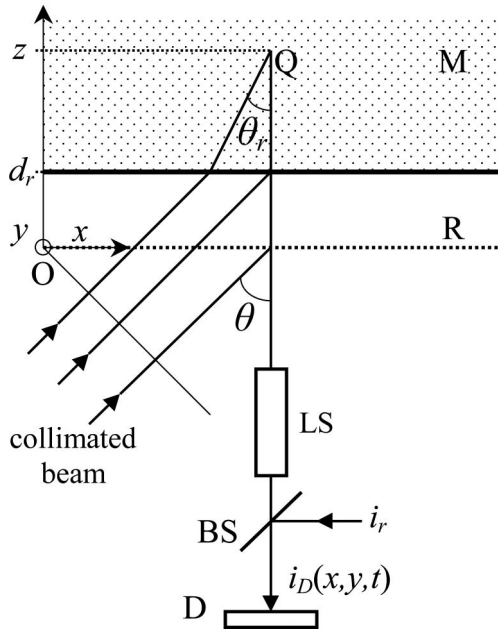

Fig. 2. Schematic diagram of the TSI system: R, reference surface placed at $z=0$ and $y \le 0$; M, material sample with refractive index n_M; Q, internal point within the sample; LS, lens system used to image M and R; BS, beam splitter; D, detector array.

(x,z) is the plane of incidence of the light. A lens system LS is used to image the sample and the reference surface on detector array D. Beam splitter BS combines the scattered light collected from the object with a plane wave i_r, which acts as the reference beam of the interferometer. The whole system is immersed into a transparent medium of refractive index $n_0=1$.

The illumination beam is refracted at the object surface $z=d_r$, reaching an internal point Q with coordinates (x,y,z) at an angle $\theta_r = \sin^{-1}(n_0\sin\theta/n_M)$ to the optical axis. The phase difference between the light scattered at Q and the reference beam can be expressed relative to the phase difference at point O as [21]

$$\phi(x,y,z) = \frac{2\pi}{\lambda}[n_0 x\sin\theta + n_0 d_r(1+\cos\theta) + n_M(z-d_r)(1+\cos\theta_r)]. \quad (11)$$

The value of $\phi(x,y,z)$ represents the deterministic phase φ_d obtained when the optical field u_i is evaluated at the input plane of an internal layer located at a distance $z-d_r$ from the object front surface [see Eq. (3)].

It is considered that illumination angle θ changes linearly with time t about central angle θ_c as

$$\theta(t) = \theta_c + \frac{\Delta\theta}{T}t, \quad (12)$$

where $\Delta\theta$ is the tilt angle and T is the duration of the image acquisition process. Hence, phase ϕ will vary as

$$\frac{1}{2\pi}\frac{\partial\phi}{\partial t} = f(x,y,z) = \frac{n_0\Delta\theta}{\lambda T}[x\cos\theta - d_r\sin\theta - (z-d_r)\xi] = f_x(x,y) + f_{d_r}(y,d_r) + f_z(y,z-d_r), \quad (13)$$

where the parameter ξ is defined by

$$\xi = \frac{\partial\theta_r}{\partial\theta}\sin\theta = \frac{\chi\cos\theta\sin\theta}{(1-\chi^2\sin^2\theta)^{1/2}}, \quad (14)$$

and $\chi = n_0/n_M$.

The phase temporal variation $f(x,y,z)$ represents the modulation frequency produced by the interference between the back-scattered light within the object and the reference wavefront coming from beam splitter BS. Despite the fact that the frequency of each term in Eq. (13) depends on θ and, consequently, changes during the acquisition process, it is assumed that $\Delta\theta$ is small enough so that the resulting frequency changes can be neglected.

At $z=d_r$, $f(x,y,z) = f_x(x,y) + f_{d_r}(y,d_r)$ is the frequency associated with a point positioned on the object surface. Considering $z=d_r=0$, $f(x,y,z) = f_x(x,y)$ is the frequency associated with a point lying on the reference surface.

The light intensity i_D measured at the detector plane is given by [21]

$$i_D(x,y,t) = i_r(x,y) + 2\int_{d_r}^{z_{\max}} [i_r(x,y)i(x,y,z)]^{1/2} \times \cos[2\pi f(x,y,z)t]\mathrm{d}z + 2\int_{d_r}^{z_{\max}}\int_{d_r}^{z_{\max}} [i(x,y,z)i(x,y,z')]^{1/2} \times \cos\{2\pi[f(x,y,z) - f(x,y,z')]t\}\mathrm{d}z\mathrm{d}z'. \quad (15)$$

The first term in Eq. (15) accounts for the dc component of the reference beam. The second term represents the intensity modulation due to the interference between the reference beam and the light scattered from the material. The third term corresponds to the cross interference between the light coming from within the object and contributes to low-frequency components of the signal. The integration limit $z_{\max}$ is determined by the object back surface, the maximum penetration depth of the light, or the depth range of the TSI system, whichever is the minimum [21].

It should be noticed that the fluctuations into the optical path of the back-scattered light introduced by the scattering centers, which are randomly distributed inside the material, produce a random positioning error in the integration variable z in Eq. (15) and slight variations in the frequencies detected. Thus, the influence of the speckle noise is implicitly considered in the evaluation of the intensity at the detector.

B. Data Processing and Depth-Resolved Phase Evaluation

The Fourier transform of the intensity signal along the time axis $i_D(x,y,t)$ gives rise to the spectrum $|I_D(x,y,f)|^2$. The magnitude of this spectrum represents the degree of scattering at any point within sample M or at reference surface R, and the frequencies are related to the position of the scattering centers by means of Eq. (13). Therefore, $|I_D|^2$ can be associated to the internal structure of the object and its position relative to the reference surface.

Figure 3(a) schematically shows the mean value of the spectrum $\langle|I_D|^2\rangle$ evaluated along the y axis for a horizontal position, and Fig. 3(b) depicts the mean spectrum over the (x,f) plane. It is observed that a peak appears at $f = 0$ for every horizontal position, a peak P_R that corresponds to the reference surface, and a band P_M associated with the semitransparent sample. The low-frequency edge of P_M is related to the front surface of M and usually has the highest amplitude of the band because of the change in the refractive index at this surface.

The position d_r of the object front surface relative to R is proportional to the frequency difference f_{d_r} between the spectral peak due to the scattering at R and at the object surface [see Eq. (13)]. This frequency difference can be evaluated from several pixels located at the same horizontal position by

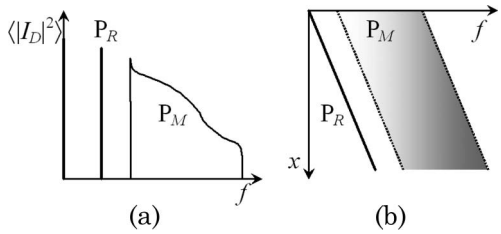

Fig. 3. Mean value of the spectrum of the interference signal $\langle|I_D|^2\rangle$ evaluated along the y axis for (a) a horizontal position and (b) over the (x,f) plane. The peak identified as P_R corresponds to the reference surface and the band P_M is associated with the semitransparent sample.

imaging either the reference or the sample. Then, the position $z(x,y)$ of a scattering point within the sample can be obtained as

$$z(x,y) = d_r - \frac{\lambda T f_z(y, z - d_r)}{\xi n_0 \Delta\theta}, \quad (16)$$

and the spectral bandwidth Δf corresponding to a thickness Δz results

$$\Delta f = -\frac{n_0|\xi|\Delta\theta}{\lambda T}\Delta z. \quad (17)$$

When a load is applied to the sample, the scattering centers will change their positions according to the mechanical properties of the material, its geometry, and boundary conditions, and the phase $\phi(x,y,z)$ will also reflect this variation. To evaluate phase ϕ at a particular point (x,y,z), it is necessary to compute the value of $\phi(x,y,f)$ from the imaginary and real parts of $I_D(x,y,f)$ and then the (x,y,f) coordinates are translated into the (x,y,z) coordinate space by means of Eq. (16).

Even though a single illumination setup as the one depicted in Fig. 2 is sufficient to detect the internal structure by evaluating the spectrum $|I_D|^2$, two illumination directions are needed to determine the horizontal in-plane u and the out-of-plane w displacement components. For right and left lateral illumination, the phase change $\Delta\phi(x,y,z) = \phi(x+u, y, z+w) - \phi(x,y,z)$ due to the displacement $\mathbf{d} = (u,0,w)$ can be evaluated as [21]

$$\Delta\phi_R(x,y,z) = \frac{2\pi}{\lambda}\{u(x,y,z)n_0\sin\theta_R + w(x,y,d_r)n_0(1+\cos\theta_R) + [w(x,y,z) - w(x,y,d_r)]n_M(1+\cos\theta_{Rr})\},$$
$$\Delta\phi_L(x,y,z) = \frac{2\pi}{\lambda}\{-u(x,y,z)n_0\sin\theta_L + w(x,y,d_r)n_0(1+\cos\theta_L) + [w(x,y,z) - w(x,y,d_r)]n_M(1+\cos\theta_{Lr})\}, \quad (18)$$

where θ_{Rr} and θ_{Lr} are the refracted angles for right and left illumination, respectively. By selecting

$\theta_R = \theta_L = \theta$, the out-of-plane $\Delta\phi_z$ and in-plane $\Delta\phi_x$ phase changes can be evaluated by adding and subtracting $\Delta\phi_R$ and $\Delta\phi_L$, respectively. Finally, the displacement components u and w can be computed as

$$u(x,y,z) = \frac{\lambda\Delta\phi_x(x,y,z)}{4\pi n_0 \sin\theta},$$

$$w(x,y,z) = \frac{\lambda\Delta\phi_z(x,y,z)}{4\pi n_M(1+\cos\theta_r)} - \frac{\lambda\Delta\phi_z(x,y,d_r)}{4\pi} \times \left[\frac{1}{n_M(1+\cos\theta_r)} - \frac{1}{n_0(1+\cos\theta_r)}\right]. \quad (19)$$

The depth resolution δz of the TSI system is defined as the minimum distance between surfaces whose corresponding interference signals can be fully resolved in the frequency domain. It can be demonstrated that the depth resolution is given by [21]

$$\delta z = -\frac{\lambda\gamma}{n_0|\xi|\Delta\theta}, \quad (20)$$

where the parameter γ is proportional to the spectral bandwidth of the window function used for evaluating the Fourier transform. In the case of rectangular or Hanning windows, $\gamma = 2$ and 4, respectively.

4. Results of the Numerical Analysis

The numerical model proposed in Sections 2 and 3 was used to simulate the intensity distribution obtained with the TSI technique. The imaging geometry and the illumination setup of the TSI system that were used in this simulation were similar to the ones shown in Figs. 1 and 2. For simplicity, it was considered that only two scattering layers existed in sample M, the object surface S_0 and the internal layer S_l, and that the scattering centers were uniformly distributed in both layers.

The simulation parameters were selected in a similar way as in the experimental work presented by Ruiz *et al.* in [21]. The refractive index of the semitransparent material was chosen as $n_M = 1.4$, a value that is typical of the epoxy resins that are usually utilized in the manufacturing of fiber glass composites. The distance between the sample and the reference surface was $d_r = 4$ mm, the depth of the internal scattering layer was $d_l = 2$ mm, the central illumination angle was $\theta_c = \pi/4$ rad, the tilt angle was $\Delta\theta = 0.0048$ rad, the wavelength was $\lambda = 532$ nm corresponding to green laser light, the size of the field of view was $7.2 \times 7.2\,\text{mm}^2$ and its spatial resolution was 256×256, and the intensities were digitized with 256 gray levels. This simulation was carried out for 256 simulated frames with an average speckle size of 2 pixels. Finally, the value of θ_c was chosen so that $|\xi(\theta)|$ is maximum and almost constant for the whole simulation [see Eq. (14)]. Consequently, the depth resolution δz was optimized [see Eq. (20)].

Two sequences of interferograms were generated considering the left and the right lateral illuminations. Then, a displacement $\mathbf{d} = (u, 0, w)$ was introduced. The out-of-plane component w was a rigid body tilt around the vertical axis y with a maximum displacement of 2 μm. The in-plane component u was a linear displacement along the horizontal axis x. In this last case, the maximum displacement at the front surface S_0 was 3 μm, and the maximum displacement at the internal slice S_l was 2 μm. Finally, the intensity distribution of each corresponding speckle interferogram of the sequence was calculated.

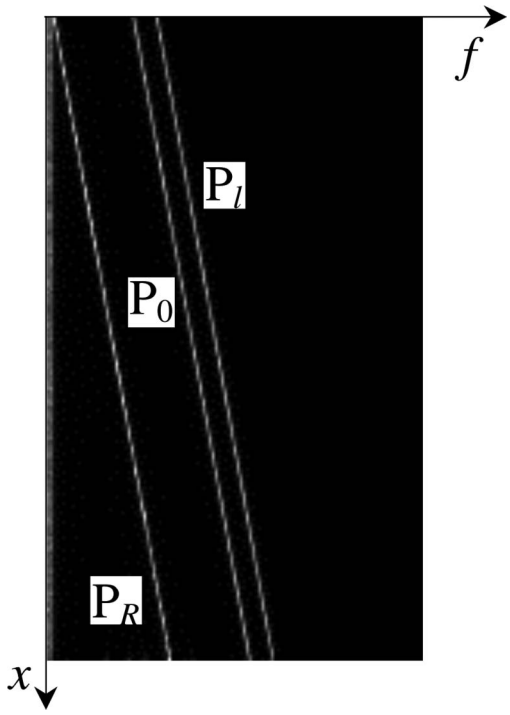

Fig. 4. Mean value of the spectrum of the interference signal evaluated along the y axis on the (x,f) plane. The peaks identified as P_R, P_0, and P_l correspond to the reference surface R, the object surface S_0, and the inner scattering layer S_l, respectively.

Figure 4 shows the mean value of the spectrum of the interference signal generated for one sequence of interferograms using the left lateral illumination. This figure displays the low-frequency peak P_R that is associated with reference surface R and also the

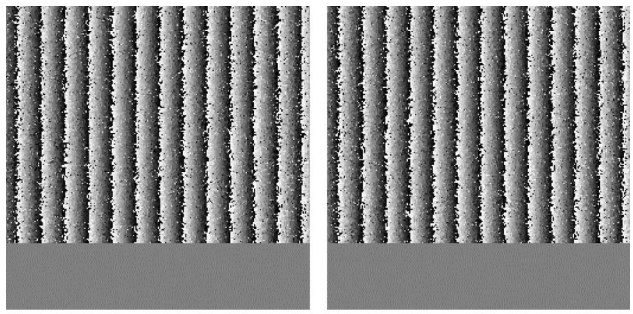

Fig. 5. Out-of-plane phase change obtained by a numerical simulation of a TSI system due to a rigid body tilt of the sample about the y axis. The wrapped phase maps correspond to (a) the front surface and (b) the slice within the material at a distance d_l from the front surface.

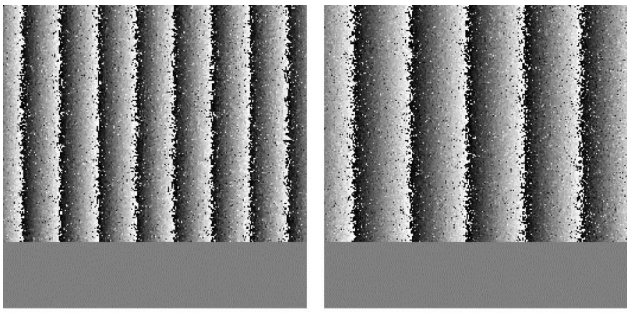

Fig. 6. In-plane phase change obtained by a numerical simulation of a TSI system due to a linear horizontal displacement applied to the sample along the x axis. The wrapped phase maps correspond to (a) the front surface and (b) the slice within the material at a distance d_l from the front surface.

two consecutive peaks P_0 and P_l, which correspond to each scattering layer of the sample, respectively. The position of the sample d_r is proportional to the bandwidth between P_R and P_0, and the frequency difference between the peaks P_0 and P_l corresponds to the depth d_l of the scattering layer S_l.

The out-of-plane wrapped phase changes due to the rigid body tilt introduced to the sample, evaluated at the front surface S_0 and at the internal scattering layer S_l, are shown in Figs. 5(a) and 5(b), respectively. The bottom area showing a uniform phase map corresponds to reference surface R. As expected, the evaluated phase change is similar for both layers and varies linearly along the horizontal direction x due to the simulated rigid body rotation introduced around the vertical axis y.

Figures 6(a) and 6(b) depict the in-plane wrapped phase changes due to the linear horizontal displacement introduced in the sample, evaluated at the front surface S_0 and at the internal scattering layer S_l, respectively. The bottom area showing a uniform phase map corresponds to reference surface R. As expected, the evaluated phase change varies linearly along the horizontal direction x for both layers and

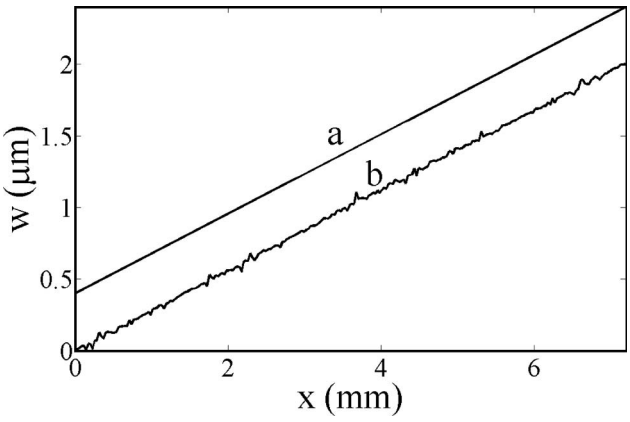

Fig. 7. Comparison between the original out-of-plane displacement component w (line a) and the displacement obtained at the internal layer S_l (line b). An offset of 0.4 μm was added to the original displacement (line a) for the sake of clarity.

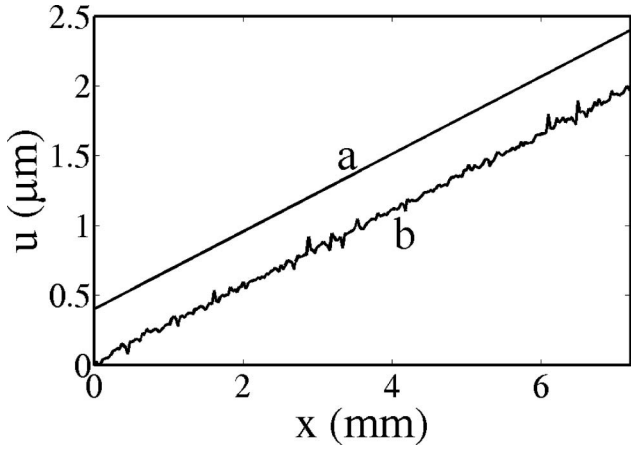

Fig. 8. Comparison between the original in-plane displacement component u (line a) and the displacement obtained at the internal layer S_l (line b). An offset of 0.4 μm was added to the original displacement (line a) for the sake of clarity.

is larger at the front surface than at the internal layer.

Finally, the internal displacement field components were evaluated by unwrapping the phase maps displayed in Figs. 5(b) and 6(b) by means of a minimum L^0-norm unwrapping algorithm [26,27]. Figure 7 shows a comparison between the original out-of-plane displacement component w (line a) and the displacement obtained at the internal layer S_l (line b). Similarly, Fig. 8 compares the original in-plane displacement component u (line a) and the displacement obtained at the internal layer S_l (line b).

5. Conclusions

We have proposed, on the one hand, a linear simulation model to compute an approximation of the subjective speckle field that is obtained with a $4f$ imaging system when a semitransparent scattering material is illuminated with monochromatic light. Under assumptions of weak scattering, no absorption, flat object surface, and uniform average refractive index in the macroscale, we produced a model that retains and simulates the fundamental properties of the speckle fields that are recorded in TSI for depth-resolved displacement measurements. On the other hand, we simulated the illumination strategy used in TSI, i.e., a linearly varying illumination angle and the interference with a reference beam, to encode depth in the temporal modulation of the speckle interferograms recorded in the image plane of the optical system. The ability of the model to detect the internal structure of a weakly scattering material and to simulate depth-resolved displacement measurements was illustrated with simple examples that included out-of-plane and in-plane deformations.

The overall model constitutes the first building block of a more complete simulation in which different phenomena could be incorporated, mainly object nonplanar geometry, material scattering and absorption, nonuniform refractive index, birefringence, and

speckle decorrelation. It will allow us to study the relative importance of these effects on the performance of the TSI technique and their associated errors.

The authors thank A. Federico for his valuable comments.

References

1. M. I. Friswell and J. E. Mottershead, *Finite Model Updating in Structural Dynamics* (Springer, 1995).
2. M. Grediac, "Principe des travaux virtuels et identification," C. R. Acad. Sci. Ser. II **309**, 1–5 (1989).
3. F. Pierron, S. Zhavoronok, and M. Grediac, "Identification of the through-thickness properties of thick laminated tubes using the virtual fields method," Int. J. Solids Struct. **37**, 4437–4453 (2000).
4. M. Grediac, F. Pierron, S. Avril, and E. Toussaint, "The virtual fields method for extracting constitutive parameters from full-field measurements: a review," Strain **42**, 233–253 (2006).
5. R. Jones and C. Wykes, *Holographic and Speckle Interferometry* (Cambridge University, 1989).
6. P. K. Rastogi, *Digital Speckle Pattern Interferometry and Related Techniques* (Wiley, 2001).
7. R. Rodriguez-Vera, D. Kerr, and F. Mendoza-Santoyo, "Electronic speckle contouring," J. Opt. Soc. Am. A **9**, 2000–2008 (1992).
8. P. Jacquot, "Speckle interferometry: a review of the principal methods in use for experimental mechanics applications," Strain **44**, 57–69 (2008).
9. A. Giraudeau, B. Guo, and F. Pierron, "Stiffness and damping identification from full field measurements on vibrating plates," Exp. Mech. **46**, 777–787 (2006).
10. S. Avril and F. Pierron, "General framework for the identification of constitutive parameters from full-field measurements in linear elasticity," Int. J. Solids Struct. **44**, 4978–5002 (2007).
11. S. Avril, F. Pierron, M. A. Sutton, and J. H. Yan, "Identification of elasto-visco-plastic parameters and characterization of Luders behavior using digital image correlation and the virtual fields method," Mech. Mater. **40**, 729–742 (2008).
12. T. Abe, Y. Mitsunaga, and H. Koga, "Photoelastic computer-tomography—a novel measurement method for axial residual-stress profile in optical fibers," J. Opt. Soc. Am. A **3**, 133–138 (1986).
13. H. Aben, A. Errapart, L. Ainola, and J. Anton, "Photoelastic tomography for residual stress measurement in glass," in *Optical Metrology in Production Engineering*, (SPIE, 2004) pp. 1–11.
14. D. D. Steele, T. L. Chenevert, A. R. Skovoroda, and S. Y. Emelianov, "Three-dimensional static displacement stimulated echo NMR elasticity imaging," Phys. Med. Biol. **45**, 1633–1648 (2000).
15. M. T. Draney, R. J. Herfkens, T. J. R. Hughes, N. J. Pelc, K. L. Wedding, C. K. Zarins, and C. A. Taylor, "Quantification of vessel wall cyclic strain using cine phase contrast magnetic resonance imaging," Ann. Biomed. Eng. **30**, 1033–1045 (2002).
16. B. K. Bay, T. S. Smith, D. P. Fyhrie, and M. Saad, "Digital volume correlation: three-dimensional strain mapping using x-ray tomography," Exp. Mech. **39**, 217–226 (1999).
17. J. Schmitt, "OCT elastography: imaging microscopic deformation and strain of tissue," Opt. Express **3**, 199–211 (1998).
18. A. F. Fercher, W. Drexler, C. K. Hitzenberger, and T. Lasser, "Optical coherence tomography—principles and applications," Rep. Prog. Phys. **66**, 239–303 (2003).
19. K. Gastinger, S. Winther, and K. D. Hinsch, "Low-coherence speckle interferometer (LCSI) for characterization of adhesion in adhesive-bonded joints," Proc. SPIE **4933**, 59–65 (2003).
20. G. Gülker, K. D. Hinsch, and A. Kraft, "Low-coherence ESPI in the investigation of ancient terracotta warriors," Proc. SPIE **4933**, 53–58 (2003).
21. P. D. Ruiz, J. M. Huntley, and A. Maranon, "Tilt scanning interferometry: a novel technique for mapping structure and three-dimensional displacement fields within optically scattering media," Proc. R. Soc. A **462**, 2481–2502 (2006).
22. J. M. Coupland and J. Lobera, "Holography, tomography and 3D microscopy as linear filtering operations," Meas. Sci. Technol. **19**, 074012 (2008).
23. J. W. Goodman, *Introduction to Fourier Optics* (McGraw-Hill, 1996).
24. S. Equis and P. Jacquot, "Simulation of speckle complex amplitude: advocating the linear model," Proc. SPIE **6341**, 634138.1–634138 (2006).
25. A. Dávila, G. H. Kaufmann, and D. Kerr, "Digital processing of ESPI addition fringes," in *Fringe '93*, W. Jüptner and W. Osten, eds. (Akademie Verlag, 1993), pp. 339–346.
26. D. C. Ghiglia and M. D. Pritt, *Two Dimensional Phase Unwrapping: Theory, Algorithms and Software* (Wiley, 1998).
27. P. D. Ruiz, G. H. Kaufmann, and G. E. Galizzi, "Unwrapping of digital speckle pattern interferometry phase maps by use of a minimum L^0-norm algorithm," Appl. Opt. **37**, 7632–7644 (1998).